# BAR-ILAN UNIVERSITY

## Human-organ-scale X-ray Fluorescence Ghost Imaging for Radioisotope-free Diagnostics

Eliyahu Levinson

Submitted in partial fulfilment of the requirements for the Master's Degree in the Department of Physics, Bar-Ilan University

Ramat-Gan, Israel 2026

This work was carried out under the supervision of

Prof. Sharon Shwartz

Department of Physics, Bar-Ilan University

# Table of Contents

Abstract ..... i

1. Introduction ..... 1

2. Background ..... 4

2.1. Nuclear Imaging ..... 4

2.2. Computational Ghost Imaging ..... 5

2.3. X-ray fluorescence ..... 7

2.4. Quantitative Evaluation Metrics ..... 8

3. Experimental and computational procedures ..... 9

3.1. Experimental procedure ..... 9

3.2. Computational procedure ..... 11

4. Results ..... 14

5. Discussion ..... 19

6. Bibliography ..... 21

**תקציר** ..... א

# Abstract

A wide range of diagnostic information in medicine is currently obtained using radioactive tracers. While central to nuclear medicine in modalities such as Positron emission tomography (PET), Single-photon emission computed tomography (SPECT) and scintigraphy, these methods are inherently constrained: radiation dose limits repeat examinations, short tracer half-lives and complex logistics restrict access and raise costs, and their relatively poor spatial resolution often necessitates complementary CT or MRI.

Although X-ray fluorescence (XRF) has been recognized as an element-specific and non-radioactive alternative, conventional implementations rely on pencil-beam raster scanning, in which a collimated, millimeter-scale X-ray beam probes the sample point-by-point, requiring sequential scanning over the entire field of view. This results in impractically long acquisition times at human-organ scales, and therefore has not been translated into clinically viable organ-scale imaging.

In this work, I present a first proof-of-concept demonstration of a non-radioactive alternative based on XRF via computational ghost imaging (CGI), an imaging method relying on spatially modulated illumination patterns rather than direct spatial resolve detection. The spatial information is encoded in the known illumination patterns and reconstructed computationally from their correlations with the measured fluorescence signals. The target object is an anthropomorphic phantom containing a thyroid insert filled with an iodine solution, serving as a model for non-radioactive tracer imaging at clinically relevant dimensions.

The experimental system utilizes an X-ray source, structured illumination patterns made of silver, and a silicon drift detector (SDD) to collect iodine Kα fluorescence (~28 keV). The structured patterns illuminate the phantom, and for each one the integrated iodine fluorescence yield is recorded. Reconstruction is performed using Noise2Ghost (N2G), a self-supervised convolutional neural network which inverts the measurement model without requiring external ground truth. Quantitative image-quality metrics, including contrast-to-noise ratio (CNR), mean square error (MSE), and Fourier ring correlation (FRC), are used to assess reconstruction quality.

Beyond this demonstration, I analyse practical pathways toward clinical feasibility. Several technical improvements could substantially reduce acquisition times. Fluorescence collection efficiency could be increased by roughly two orders of magnitude by replacing the single detector used in this work with an array of CdTe detectors, providing a much larger area coverage and near-unity efficiency. In contrast, the SDD used here operated at 13% efficiency. Spectral matching between the excitation source and the fluorescence transition could significantly increase fluorescence yield - tuning the incident x-ray spectrum near the Iodine K-edge rather than using a broad bremsstrahlung spectrum, acquisition times can be reduced by several orders of magnitude. Advances in compressive or machine-learning-based reconstruction could reduce acquisition times by an additional order of magnitude. These suggest a realistic route toward organ-scale, non-radioactive functional imaging with clinically relevant acquisition times.

# 1. Introduction

Medical imaging plays a central role in modern diagnosis and treatment planning, providing non-invasive insight into the structure and functions of the human body. A wide range of imaging modalities have been developed, including anatomical techniques such as Computed Tomography (CT), Magnetic Resonance Imaging (MRI), Ultrasound, as well as functional imaging techniques that visualize physiological and metabolic processes. Among the latter, nuclear medicine methods play an important role because of their ability to assess biochemical activity in vivo.

In nuclear medicine, modalities such as scintigraphy, SPECT and PET are routinely used to track metabolic processes and selective accumulation in specific tissues using radioactive tracers. These methods have become indispensable in fields such as oncology and cardiology [1-5], where they provide quantitative information that assists with diagnosis, monitoring, and treatment planning.

Despite their clinical importance, all nuclear imaging methods share a fundamental dependence on radioactive isotopes. They rely on the spontaneous decay of unstable nuclei, either through direct gamma emission or positron annihilation. This reliance on radioactive decay imposes unavoidable physical and practical constraints. Exposure to ionizing radiation increases the risk of cancer and other diseases, limiting the permissible dose and restricting the frequency of repeated examinations [6,7]. Because of this, the half-lives of clinical radiotracers typically range from several hours to days, creating major logistical challenges in isotope production, transport and storage [8,9], contributing significantly to cost and limiting accessibility.

Moreover, nuclear imaging techniques are constrained by spatial resolution. Under clinical conditions, the typical resolutions of PET (4-5 mm) and SPECT (8-10 mm) are often insufficient and are compensated for by using hybrid imaging systems with computed tomography (CT) (as shown in Fig. 1) or magnetic resonance imaging (MRI) [9,10], leading to additional cost and complexity. While advances in reconstruction algorithms have been made [11-14], they cannot circumvent the intrinsic limitations of radioactive decay.

These challenges motivate the search for alternative approaches to functional imaging that avoid radioactive tracers all while preserving diagnostic sensitivity and spatial resolution. One

promising direction is based on XRF, where incident X-rays excite inner-shell electrons in atoms within the sample, and the subsequent emission of characteristic fluorescence photons provides an element-specific signature.

Because fluorescence emission is directly tied to the elemental composition, XRF enables quantitative mapping of elemental distributions in a way that is analogous to nuclear imaging, but without reliance on radioactive decay. A key distinction between XRF-based and nuclear-based imaging is that fluorescence emission occurs only during external excitation. Once the excitation is ceased, no further radiation is emitted. This property fundamentally changes the radiation-risk profile and removes the logistical challenges associated with radioactive isotopes.

In this work I present an alternative algorithmic approach for spatial elemental mapping via the Ghost Imaging method (GI). In particular, Computational Ghost Imaging (CGI) replaces the limitations of point-by-point XRF raster scanning with structured illumination and algorithmic reconstruction [15]. Instead of measuring spatially resolved signals directly at each point, CGI correlates a known sequence of illumination patterns with a sequence of corresponding signals to recover the spatial distribution of interest. In the context of XRF, the total fluorescence yield measured is correlated with its corresponding illumination pattern to eventually reconstruct the desired elemental map [16].

I demonstrate the extension of XRF-CGI to the scale of human organs, with the target object for reconstruction being a thyroid insert filled with an iodine solution, encased within an anthropomorphic phantom. My work shows that correlating structured illumination with their respective Iodine fluorescence signal via CGI can recover the spatial distribution of the solution within the phantom with a resolution of ~4 mm. The results presented here establish a general framework for non-radioactive tracer imaging and suggest a pathway toward safer, repeatable, and more accessible diagnostic modalities.

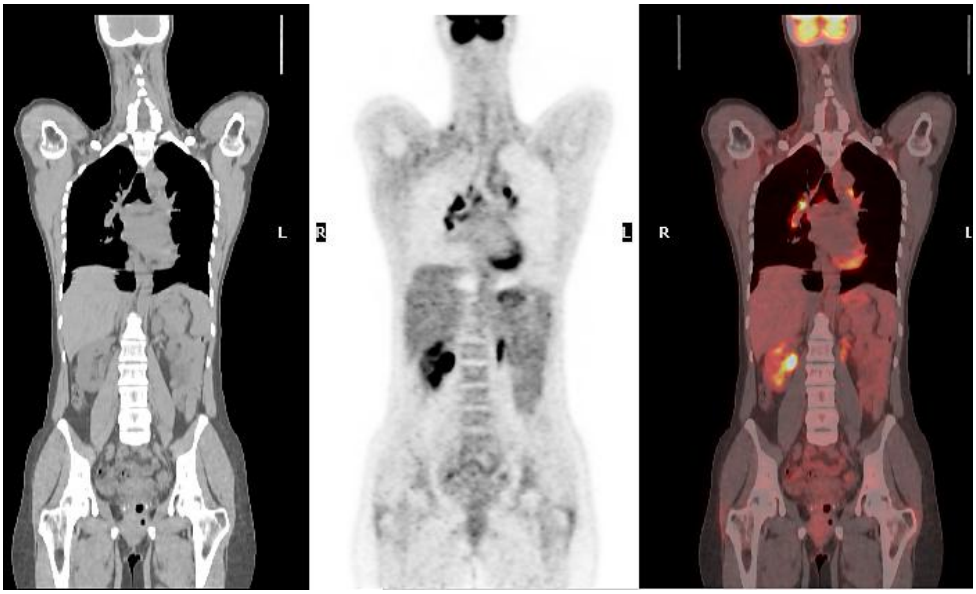



**Fig. 1.** Different scans of the human body [17]. From left to right: Computed Tomography (CT), Positron Emission Tomography (PET), and the corresponding hybrid PET-CT image. The CT scan provides high-resolution anatomical information, while PET imaging reflects metabolic activity through radiotracer uptake. The combined PET-CT image enables precise localization of activity by overlaying it onto the detailed anatomical information. Regions of increased intensity correspond to elevated metabolic activity and may indicate the presence of a tumour.

# 2. Background

## 2.1. Nuclear Imaging

Nuclear medicine imaging comprises a family of functional imaging techniques in which a biologically active compound is labelled with a radionuclide and administered via injection, inhalation, or oral ingestion. The spatial distribution of the tracer can be inferred from the gamma rays emitted during the nuclear decay, allowing physiological processes such as metabolism and receptor binding to be visualized in vivo. The simplest implementation of this approach is Planar scintigraphy, in which a gamma camera records two-dimensional projection images of tracer uptake. Building on this concept, SPECT acquires projection images from multiple angles using collimated detectors and reconstructs them into a three-dimensional distribution of tracer activity. PET is a complementary technique which employs positron-emitting tracers such as Fluorine-18 [18]. In PET, the emitted positron annihilates with a nearby electron, producing a pair of 511 keV photons that are detected in coincidence. This detection scheme enables higher sensitivity and more quantitative tomographic imaging compared with single-photon techniques. In modern clinical practice, PET and SPECT are commonly combined with anatomical imaging modalities such as CT or Magnetic Resonance Imaging (MRI) [9,10] to provide complementary information, combining functional tracer uptake with high resolution anatomical localization and enabling attenuation correction during image reconstruction.

Despite nuclear imaging being a gold standard for in vivo functional and molecular imaging, a safer and less complicated logistic-wise imaging approach may be achieved with the XRF modality. Early studies explored the application of XRF in medical imaging and have demonstrated that element-specific contrast could be obtained in humans at clinically acceptable doses [19]. Despite its conceptual appeal, conventional XRF has not been adopted for human-organ scale medical imaging. Due to its isotropic nature, Traditional XRF imaging relies on raster scanning with a narrow pencil beam, measuring fluorescence point by point. While this approach can achieve high spatial resolution, the acquisition times scale exceedingly with the field of view, making it impractical for human-scale imaging [20]. Therefore, it has largely remained confined to small samples or preclinical animal studies, and extending it to human-organ scales poses formidable challenges [21].

## 2.2. Computational Ghost Imaging

Computational Ghost imaging (CGI) is a method used in this work to reconstruct the 2D distribution of the iodine solution without capturing it through direct imaging methods.
In its original form, Ghost Imaging (GI) was based on quantum correlations [22], involving a pair of entangled photons generated from a single source. One photon encounters a multi-pixel detector, and the other encounters the object or is detected by a single-pixel (bucket) detector. The multi-pixel registers only photons whose counterpart reached the bucket. By correlating the intensities registered in both detectors for each pair of photons, the image of the object can be reconstructed. It was later shown that GI can be done without the need for quantum entanglement, instead relying on classical correlations between light patterns and their respective energies [18]. A different approach to this method is CGI, which essentially disregards the need for a multipixel detector and uses only the bucket detector.

For XRF-CGI, the general experimental procedure is as follows:
First, the realizations are generated. In the case of X-ray imaging, this can be done by pre-scanning a larger illumination pattern at different sections or by computer-generating them, as there are currently no spatial light modulators (SLM) available for X-rays. The object is then presented to the system and irradiated by X-rays that initially pass through a realization [23]. The object will fluoresce isotropically, with some incident photons reaching the bucket detector for each applied realization. The correlation between the set of patterns and their corresponding fluorescent intensities allows us to reconstruct the object through various computational algorithms. In contrast to absorption, where the object can be equivalently positioned on either side of the realizations, in XRF CGI it must be placed upstream.

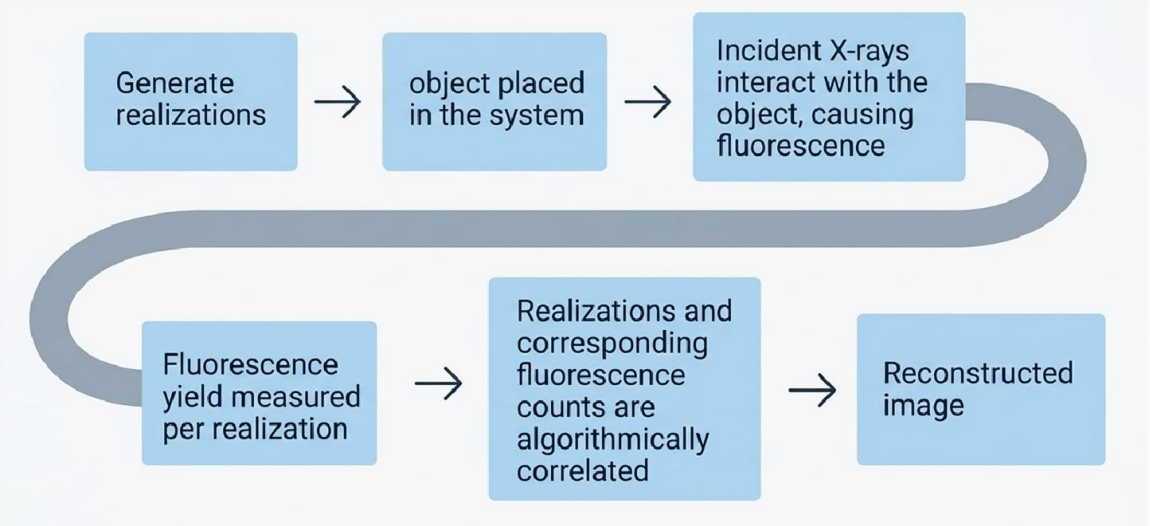



**Fig. 2.** A schematic of the XRF-CGI procedure

In general, CGI can be described in the following way:

$$y = Wx + \epsilon, \quad (1)$$

Where y is the vector of measured bucket fluorescence counts, W contains the applied realizations, x is the unknown elemental distribution, and $\epsilon$ is random uncorrelated noise. In practice, W is a matrix and each of its rows is one of the illumination patterns. The illumination patterns are either generated computationally or experimentally characterized prior to the measurement. For each illumination pattern in W, a single bucket fluorescence measurement is acquired, forming the corresponding element in y. The elemental distribution x is then estimated by solving the inverse problem defined by Eq. (1).

In the framework of compressive CGI, the system described via Eq. (1) is typically underdetermined, meaning the number of measurements is smaller than the number of unknowns. To enable accurate reconstruction in this scenario, prior information about the structure of the object is incorporated - it is commonly assumed that the object is sparse or compressible in some domain. It may be sparse in a transform space such as Fourier, wavelet basis, or in the gradient domain, where the image is assumed to be largely smooth. For the latter case, an example algorithm such as total variation (TV) regularization can be employed,

promoting sparsity of the image gradients while preserving sharp edges [24]. Specifically, TV regularization penalizes the total magnitude of intensity variations between neighbouring pixels, thereby suppressing noise while maintaining edge information.
The reconstruction is therefore obtained by solving Eq. (1) together with an additional sparsity-promoting constraint. The main advantage of this compressive approach is that it enables a sufficiently accurate image recovery using fewer realizations, reducing acquisition times. However, this comes at the reliance on the validity of the assumed sparsity model, which may not hold for all objects and can lead to reconstruction artifacts or loss of fine details.

## 2.3. X-ray fluorescence

The phenomenon of X-ray fluorescence (XRF) was first systematically studied in the beginning of the 20th century, most notably by Henry Moseley [25], showing that the energies of secondary X-ray emissions of an element are uniquely linked to its atomic number.

XRF refers to the emission of characteristic X-ray photons from a material after initially absorbing high-energy X-rays. When an atom in the material is excited by the initial X-ray photon, an electron is ejected from the inner shells, creating a vacancy. To bring the atom back to its unionized state, an electron from a higher energy shell transitions to fill the vacancy. During the relaxation process an X-ray photon is released with energy corresponding to the gap between the shells in the atom. These characteristic emissions form spectral signatures that are unique for each element, making XRF a powerful modality in various fields. The fluorescence occurs only if the incident photon energy exceeds the binding energy of the shell being ionized. Specifically in Iodine, excitation above the K-edge produces characteristic K-shell emission, with the dominant line typically detected in the Kα region (~28 keV). In material analysis, XRF assists in identifying and quantifying elements present in alloys, minerals, and environmental samples [26-28]. In the studies of art and archaeology, it is particularly valuable for non-destructive analysis of pigments and materials used by artists, aiding in the preservation of historical works [29 – 32]. In biomedicine, the method is used to map trace elements within tissues and organs, providing information on elemental distributions associated with physiological processes and uptake of contrast agents [33,34]. Due to its ability to detect trace elements with high energy resolution, XRF is well suited for element-specific

imaging, providing a contrast mechanism comparable to nuclear-based methods while avoiding the need for radioactive isotopes.

## 2.4. Quantitative Evaluation Metrics

To quantitatively evaluate reconstruction quality, complementary metrics were used: mean squared error (MSE), contrast-to-noise ratio (CNR), and Fourier ring correlation (FRC). These metrics probe different and largely independent aspects of image quality. Using all three provides a more complete and robust assessment than any single metric alone.

### MSE

MSE is used to quantify the average squared difference between two reconstructed images, providing a measure of overall reconstruction accuracy. Its main advantage lies in its simplicity and its sensitivity to global deviations, making it well suited for monitoring convergence as the number of realizations increases. However, MSE does not account for structural image quality and is insensitive to the spatial distribution of errors.

### CNR

This metric quantifies how well a feature can be distinguished from the background in the presence of noise and is therefore closely related to the detectability of structures in the image. It is relevant for assessing whether reconstructed features are not only present, but also reliably observable. Despite this, CNR depends on manual region selection and is therefore not fully objective. Moreover, it does not provide information about spatial resolution or overall reconstruction accuracy.

### FRC

Unlike MSE and CNR, which operate in real space, FRC evaluates image quality in the frequency domain and directly reflects the ability of the XRF-CGI reconstruction process to resolve fine spatial details. High correlation at a given spatial frequency indicates that structures at that scale are reliably reproduced rather than dominated by noise. Its main strength lies in its independence from external references. Nonetheless, it relies on data partitioning and on empirically defined thresholds [35], which may influence the reported spatial resolution.

Additional details for these metrics are provided in the Computational Procedure section.

# 3. Experimental and computational procedures

## 3.1. Experimental procedure

A schematic of the experimental setup is shown in Fig. 3. The CGI method is implemented in XRF by illuminating a thyroid phantom with a sequence of known structured patterns and recording the corresponding fluorescence bucket signal. Structured illuminations are

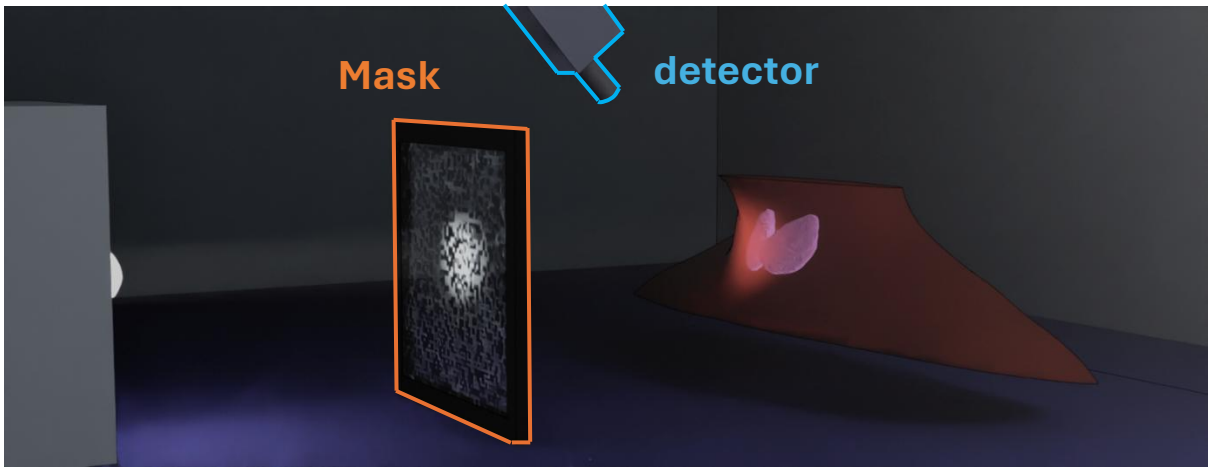



**Fig. 3.** A schematic of the experimental system. Incident x-ray photons pass through the mask and excite the iodine solution within the thyroid phantom, generating characteristic fluorescence emission. The emitted fluorescence photons are collected by the detector, which discriminates the iodine fluorescence lines from the scattered background.

generated using a binary amplitude mask mounted on a motorized translation stage upstream of the phantom. Each time a different partially overlapping sub-region of the mask is illuminated, producing a distinct intensity pattern on the phantom. The incident X-rays excite the iodine in the thyroid insert, generating characteristic fluorescence photons. The fluorescence is measured using a silicon drift detector (SDD), a semiconductor detector in which incident X-ray photons generate electron-hole pairs on a silicon surface and an internal electric field drifts the charge towards a small collecting anode, enabling energy resolved photon detection at low capacitance. The detector is positioned at approximately 45° with respect to the incident beam. For each realization, an energy spectrum is recorded, and the

iodine fluorescence signal is computed by integrating counts in the iodine K$\alpha$ window (~28.0 ± 1.0 keV) as seen in Fig. 4.

The phantom-mask distance is a few cm, being as close as possible to prevent overlap of adjacent features in the pattern. The SDD is placed 14 cm from the phantom to balance primary fluorescence signal and scattered background, and the X-ray beam footprint at the mask plane is roughly 7x5 mm².

The phantom is tilted upward by approximately 45° relative to the incident beam. This orientation was chosen to provide a clear line-of-sight from the insert to the SDD, so fluorescence photons generated across the thyroid volume would reach the detector with minimal self-attenuation and geometric occlusion.

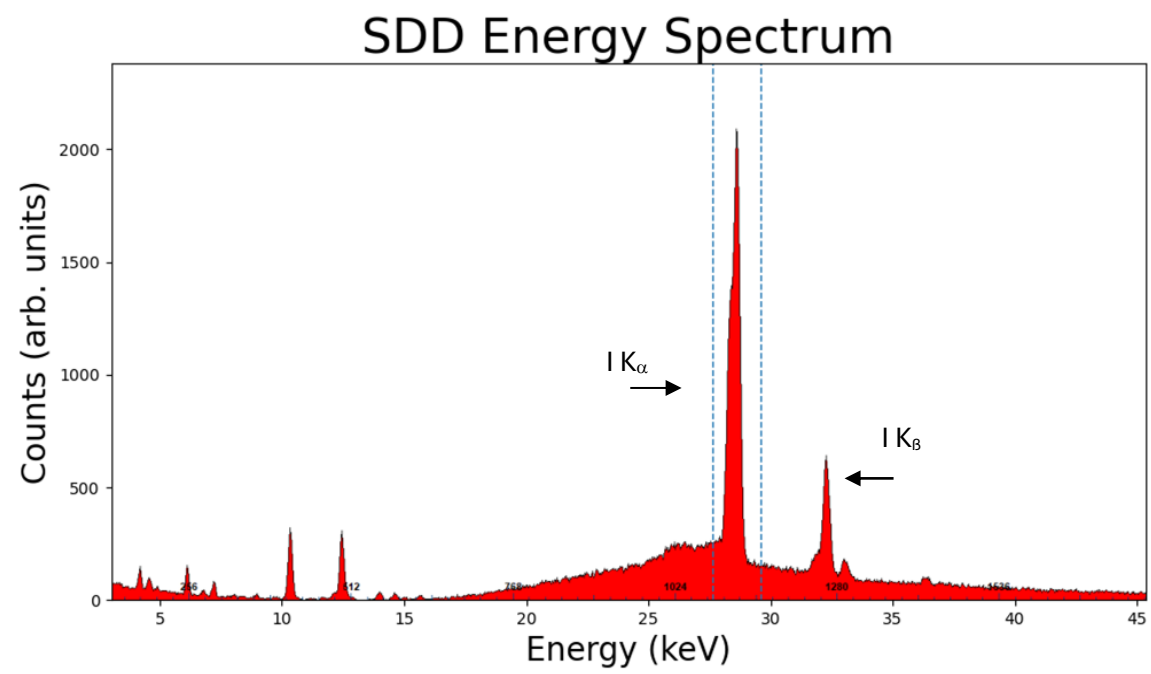



**Fig. 4.** The SDD energy spectrum. The reconstruction energy window (dashed lines) is indicated. The iodine $K_\alpha$ and $K_\beta$ fluorescence lines at 28.6 KeV and 32.3 KeV, respectively, are visible. Weaker Pb L-shell fluorescence peaks at lower energies are also observed, originating from surrounding shielding. The broad background around the $K_\alpha$ signal is primarily caused by scattered photons from the phantom, dominated by Compton scattering.

The binary mask consists of a 1.5 mm-thick Ag plate patterned with 0.5x0.5 mm² openings over a 16x16 cm² area, fabricated using high-precision 3D printing [36, 37] (open fraction is ~50%). The object is an anthropomorphic phantom (RSD Inc.) containing a thyroid insert filled with a 200 mg/mL solution of sodium diatrizoate hydrate – a common compound used

as a contrast agent. The insert area is 7.5x6 $cm^2$, representing a human-scale organ. The detector used for fluorescence measurements is an Amptek fast SDD. The x-ray source is operated at 80 kVp and 2 mA. The XRF-CGI reconstruction algorithm I chose to work with is detailed below.

## 3.2. Computational procedure

The reconstructions presented in this work were obtained using Noise2Ghost (N2G), a self-supervised convolutional neural network (CNN) method for CGI [38]. N2G partitions the realizations into subsets to form sub-reconstructions and trains a CNN to transform those sub-reconstructions such that they match independent measurements in the forward model.

Considering the model introduced in Eq. (1), N2G seeks a neural network parametrization $\hat{\theta}$ that minimizes the following expression:

$$\hat{\theta} = \underset{\theta}{\operatorname{argmin}} \ \frac{1}{2}\sum_k \sum_{i \neq k} ||W_i N_\theta(x_k) - y_i||_2^2 + \lambda R\big(N_\theta(x_k)\big), \qquad (2)$$

where the indices i and k refer to different measurement subsets and related sub-reconstructions, and K is the number of subsets. The final reconstruction is obtained by averaging the network outputs for all subsets:

$$\hat{x} = \frac{1}{K}\sum_k N_{\hat{\theta}}(x_k), \qquad (3)$$

To accelerate post-acquisition processing and to assess how much spatial information could be discarded before the reconstruction quality noticeably degraded, I implemented binning to the reconstructions. Prior to the reconstruction process, binning is applied to the original realizations while the fluorescence data remains unchanged. N2G is then applied using the binned patterns.

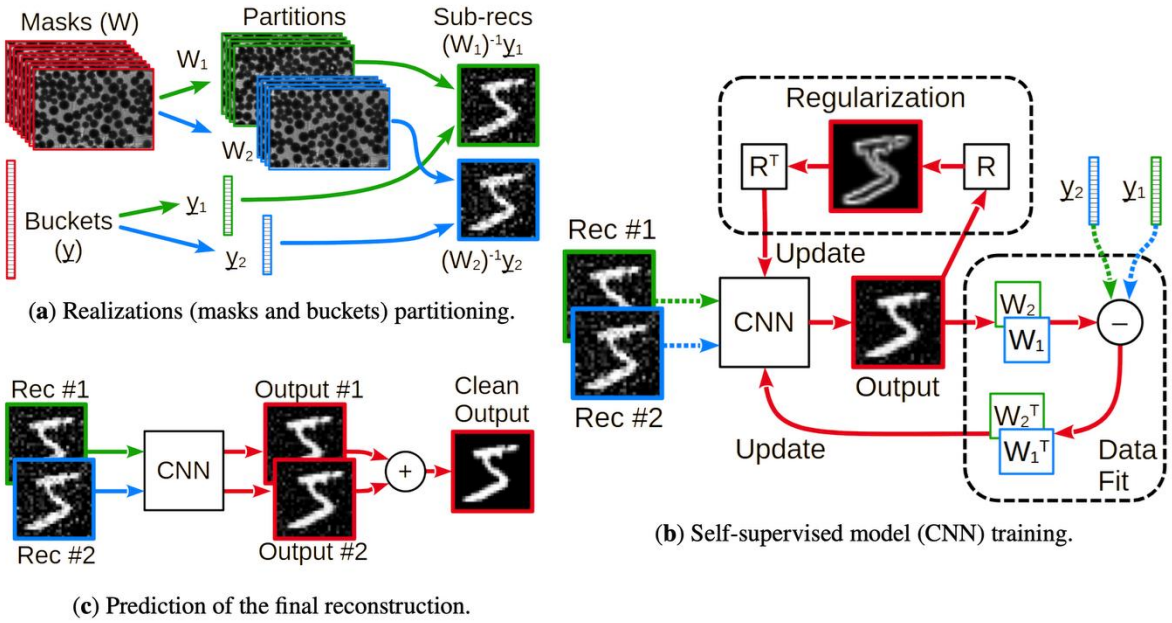



**Fig. 5.** A schematic of the N2G method [38].

This reconstruction method includes several tuneable parameters that affect reconstruction fidelity. These were selected based on empirical evaluation over a limited range of values. A comprehensive optimization was not performed due to computational limitations, as each reconstruction is computationally intensive. The chosen parameters were found to provide a reliable performance and were therefore used for reconstructions. Table 1 lists the values I used for the data shown in Figs 6, 9.

| **Parameter** | **Binning x1** | **Binning x16** |
|---|---|---|
| Num. of features | 20 | 20 |
| Num. of levels | 3 | 3 |
| Regularization value | 2e-06 | 2e-06 |
| Num. of permutations | 3 | 5 |
| Num. of splits | 4 | 5 |
| Epochs | 3072 | 3072 |
| Learning rate | 0.001 | 0.001 |

**Table 1**. N2G Hyper-Parameters used for the reconstructions.

To quantify the reconstruction quality, I use MSE, CNR, and FRC.

For the MSE, the deviations between corresponding pixels in the reconstructed and reference images are computed as:

$$MSE = \frac{1}{N} \sum_{j=1}^{N} \left(I_j - R_j\right)^2, \quad (4)$$

where $I_j$ and $R_j$ denote the intensity values of the reconstructed and reference image pixels, respectively, and N is the number of pixels. Because an external ground-truth image is unavailable, the reference image is defined as the average of five independent N2G reconstructions obtained using 5000 realizations. The MSE therefore measures convergence toward this stable reference.

To quantify contrast, I computed the CNR, which accounts for the signal and background levels as well as signal variability:

$$CNR = \frac{|S_A - S_B|}{\sigma_A}, \quad (5)$$

where $S_A$ and $S_B$ are the mean intensities in the signal and background regions, respectively, and $\sigma_A$ is the standard deviation within the signal region. I normalized by $\sigma_A$ rather than the background standard deviation because the background level decreases strongly with the number of realizations, which would artificially inflate the CNR at large realization numbers.

FRC is used as an independent and objective estimate of spatial resolution. Two reconstructions obtained from statistically independent sets of realizations are Fourier-transformed, and their normalized cross-correlation is computed over concentric rings in Fourier space as a function of spatial frequency r:

$$FRC(r) = \frac{\sum_{i \in r} \boldsymbol{F_1}(\boldsymbol{r_i}) \boldsymbol{F_2}(\boldsymbol{r_i})^*}{\sqrt{\sum_{i \in r} |\boldsymbol{F_1}(\boldsymbol{r_i})|^2 \sum_{i \in r} |\boldsymbol{F_2}(\boldsymbol{r_i})|^2}}, \quad (6)$$

where $F_1$ and $F_2$ are the Fourier transforms of the two reconstructions, and the summation is performed over all Fourier pixels $r_i$ on a ring of radius r. The resolution is defined as the spatial frequency at which the FRC curve crossed the 0.143 threshold, a commonly used empirical criterion [36].

# 4. Results

In Fig. 6a I demonstrate human-scale XRF-CGI, showing the reconstruction of the thyroid insert filled with an iodine solution that is embedded within the anthropomorphic phantom. For comparison and validation, Figs. 6b and 6c show the corresponding flat panel detector (FPD) transmission images of the isolated thyroid insert and of the entire phantom, respectively. The

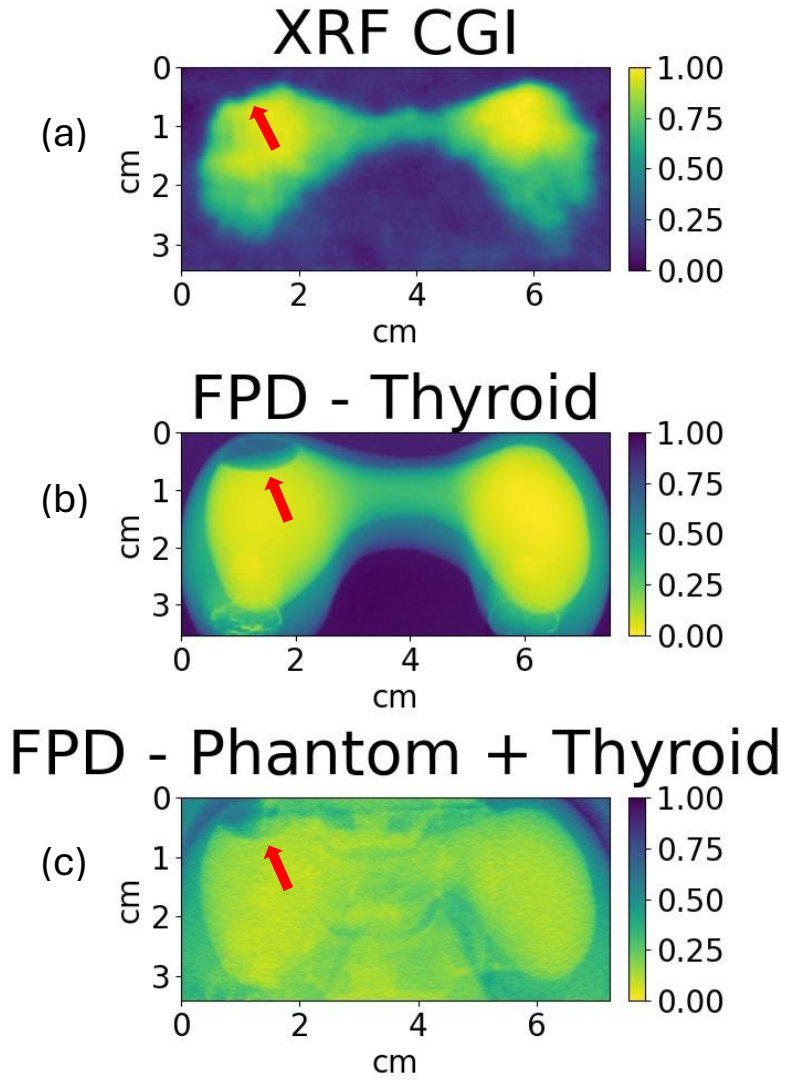



**Fig 6.** Images of the thyroid phantom filled with the iodine solution. (a) XRF-CGI reconstruction obtained using the self-supervised N2G approach with 5000 illumination realizations, demonstrating faithful recovery of the thyroid insert structure (b) Transmission Flat-panel-detector (FPD) image of the thyroid insert measured separately from the phantom. (c) FPD transmission image of the complete anthropomorphic phantom.

XRF-CGI reconstruction accurately recovers the thyroid geometry and internal structure and is consistent with the transmission reference. Notably, the thyroid is more clearly depicted in the fluorescence reconstruction than in the transmission image of the full phantom. This difference reflects the intrinsic selectivity of XRF: the fluorescence signal originates primarily from iodine-containing regions, whereas transmission imaging integrates attenuation from all tissues along the beam path. As a result, XRF-CGI naturally suppresses anatomical background and isolates the elemental distribution of interest. In the upper left region of the thyroid (indicated by arrows in all panels of Fig. 6), a small missing section is visible, especially in the isolated insert and in the XRF-CGI reconstruction. This feature originates from an air bubble trapped during filling of the cavity with the iodine solution. This resolve highlights the ability of XRF-CGI to capture internal inhomogeneities within a human-scale organ phantom.

Having demonstrated the capability of the CGI method to map the thyroid insert, I next quantify its spatial resolution. Fig. 7a shows one-dimensional profiles through the center of the thyroid insert, extracted from the FPD reference image (Fig 6b) and from the N2G reconstruction. The two profiles exhibit nearly identical shapes of the thyroid lobes, confirming an accurate recovery of the iodine distribution. Agreement is obtained both on the organ scale and for internal features: the separation between the two thyroid lobes is 45.2 ± 0.2 mm in the reference image and 44.7 ± 4.5 mm in the reconstruction. The air bubble void has a horizontal width of 9.0 ± 0.2 mm in the reference and 8.2 ± 4.5 mm in the reconstruction. Small differences are to be expected: XRF-CGI is selective to iodine-bearing regions, whereas transmission integrates attenuation over the entire thyroid volume, including the surrounding tissue.

To provide an additional quantitative and independent estimate of spatial resolution, Fig. 7b presents the Fourier Ring Correlation (FRC) curve computed between two N2G reconstructions, each obtained from 3000 independent realizations. Using the standard FRC threshold criterion, I obtained an effective spatial resolution of approximately 4.5 mm. This value is consistent with the smallest resolved features in Fig. 6 and with the profile comparison in Fig. 7a, confirming that the reconstruction retains millimeter-scale structural information across the human-scale field of view.

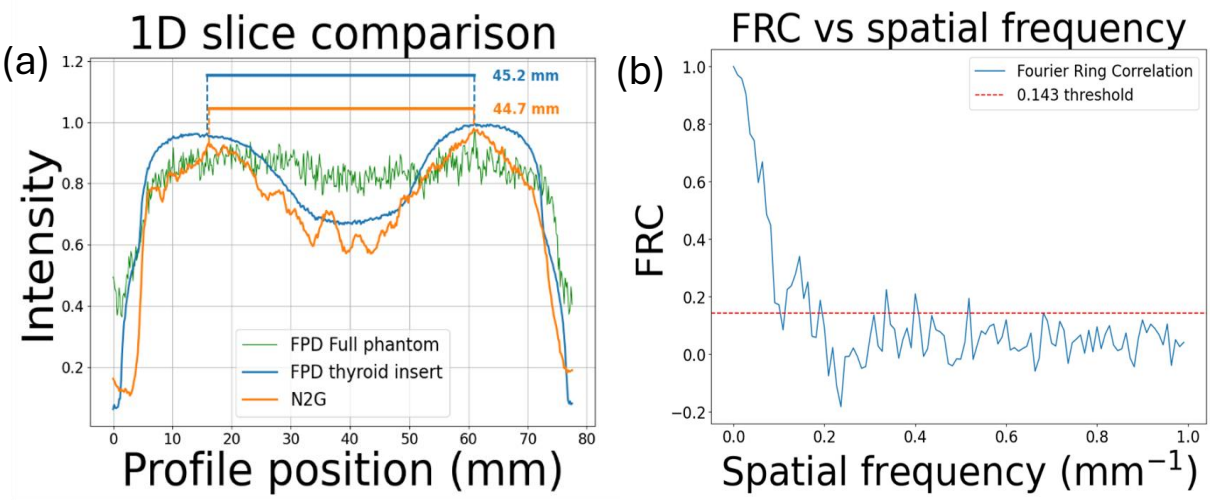



**Fig 7.** (a) One-dimensional profiles through the center of the thyroid. Shown are line extracted from the FPD image of the complete phantom, the FPD image of the thyroid insert separate from the phantom, and from a N2G reconstruction. The profiles of the isolated thyroid and the N2G reconstruction exhibit closely matching shapes and similar widths, with lobe separations of 45.2 mm and 44.7 mm, respectively, demonstrating strong agreement between the fluorescence-based reconstruction and the reference transmission measurement. (b) Fourier Ring Correlation (FRC) between two independent ghost-imaging reconstructions (solid line). The dashed red line indicates the 0.143 threshold. The first crossing occurs at 0.109 $mm^{-1}$, giving a spatial resolution of approximately 4.5 mm.

Seeing that high-quality images can be demonstrated under these conditions, I next quantify how the image quality scales with the number of mask realizations, which directly determines the ionizing-radiation dose in XRF-CGI. In Fig. 8a,b I show the dependence of the Contrast-to-Noise Ratio (CNR) and Mean-square-error (MSE) on the number of realizations, for data without binning and with a binning ×16 factor. As seen in Fig. 8a, both cases follow the same overall trend, although the binned data yield higher CNR at low realization counts. In Fig. 8b, the binned data exhibit a somewhat faster decrease in the initial stages. Beyond this initial drop, however, the curves converge to similar values, indicating that even with substantial binning the reconstruction quality was not compromised in this experiment.

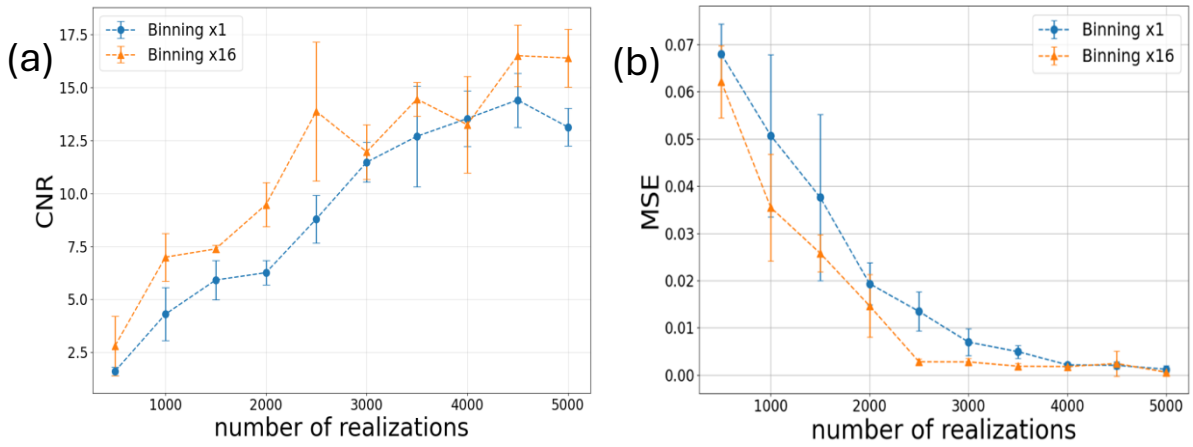



**Fig. 8.** Dependence of (a) Contrast-to-Noise Ratio (CNR) and (b) Mean-square-error (MSE) on the number of realizations. Each data point represents the mean of five independent reconstructions for a given number of realizations, and different colors denote distinct binning factors. Lines are guides to the eye. Error bars denote standard deviation.

To further illustrate the dependence of the image quality on the number of realizations, Fig. 9 shows reconstructions obtained with increasing numbers of illumination realizations. Image quality improves monotonically as additional realizations are acquired, with thyroid boundaries and internal features becoming progressively clearer. These examples visually corroborate the CNR and MSE trends and highlight the acquisition-quality trade off that sets the dose requirements of XRF-CGI.

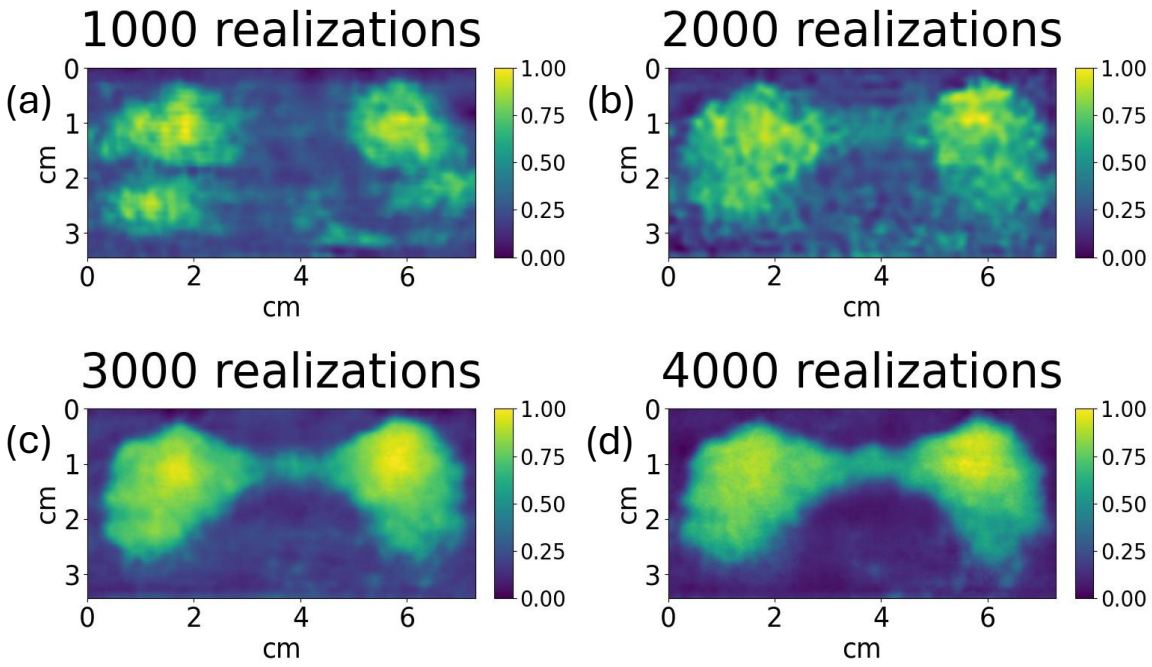



**Fig. 9.** Dependence of the N2G reconstructions on the number of realizations. Reconstructions of the thyroid phantom are shown for (a) 1,000, (b) 2,000, (c) 3,000, and (d) 4,000 realizations. The two thyroid lobes are discernible even at low realization counts, and image quality improves progressively with additional realizations. All images are displayed using normalized intensity scales.

# 5. Discussion

My research demonstrates a human-organ-scale execution of XRF-CGI with a thyroid phantom, establishing a proof-of-concept for retrieving the spatial distribution of non-radioactive markers in clinically sized organs. A clear indicator of the reconstruction's fidelity is the visibility of the air bubble within the thyroid insert: despite non-ideal, early-stage implementation, the reconstruction resolves a local inhomogeneity within the distribution. This sensitivity suggests that XRF-CGI can capture structural variations at human scale.

Because non-radioactive tracers can, in many cases, be chemically analogous to their radioactive counterparts, XRF-CGI has the potential to provide functional information like PET or SPECT while eliminating the logistical burden and radiation-related health risks associated with radioisotopes. Moreover, XRF-CGI [19] and CGI via Compton scattering [37] have been shown to produce images with spatial resolution approaching that of CT. This could reduce reliance on CT complementary assistance, which is routinely used due to the limited spatial resolution of PET/SPECT, thereby lowering overall patient dose.

To turn my proof-of-concept work into a clinically practical modality, both acquisition time and dosage must be addressed. I estimate the measurement time and dose based on current parameters and realistic upgrades to the hardware that can be implemented. For the results presented here, I acquired 5000 realizations with 20 s per realization, giving a total acquisition time of nearly 30 h, clearly beyond any clinical workflow. This long duration is primarily dictated by limited fluorescence collection efficiency. the SDD used here has an energy resolution of 125 eV, enabling clear separation of characteristic fluorescence peaks in the measured spectrum. However, it has an efficiency of only ~13% at the iodine Kα fluorescence line (~28 keV) and an active area of 17 $mm^2$. Replacing it with modern CdTe detector arrays, comprising 20 elements, with near unity efficiency at 28 keV and an effective area of 340 $mm^2$, would increase the collected fluorescence yield by a factor of ~150, reducing acquisition time proportionally. Additional reductions could be obtained by decreasing the detector-phantom distance, which increases the detected rate approximately with the inverse square of the distance. However, operating at shorter standoff requires careful optimization to control scattered-radiation backgrounds (especially in anatomically heterogeneous settings) and to mitigate dead time through appropriate choices of shaping time and front-end electronics.

An additional bottleneck is spectral mismatch between the excitation spectrum and the iodine absorption edge. The current tube was operated at 80 kVp, which provided an optimal Signal-to-Noise Ratio (SNR) in the present setup. Despite this, it is not optimized for iodine excitation. It is estimated that only 5% of the source spectrum contributes effectively, and geometric constraints applied to reduce background further reduce the flux that reaches the target thyroid. Shifting to an excitation spectrum centred around 40 keV and using filtration that suppresses non-contributing photons while transmitting those above the iodine K-edge [40] can increase the fraction of photons effectively driving fluorescence by nearly two orders of magnitude. Finally, continued progress in reconstruction, particularly via advanced machine-learning or compressive strategies, can further decrease the number of realizations needed for high-fidelity reconstructions by an additional order of magnitude.

Taken together, these improvements indicate a realistic pathway toward clinically relevant acquisition times on the order of seconds, comparable or potentially faster than current nuclear-medicine protocols, while using radioisotope-free tracers. Looking further ahead, quasi-monochromatic sources such as inverse-Compton systems could further increase the spectral efficiency and reduce dose [41], potentially pushing acquisition times below today's state-of-the-art functional imaging while preserving the key safety advantage of eliminating radioactive decay.

It is important to note that XRF-CGI is not specific to the thyroid or to iodine. In principle, it can be generalized to other organs and to a broad class of non-radioactive markers, including elements for which no suitable clinical radioisotope exists today.

# 6. Bibliography


[1] O. Manabe, T. Kikuchi, A. J. H. A. Scholte, M. El Mahdiui, R. Nishii, M.-R. Zhang, E. Suzuki, and K. Yoshinaga, Radiopharmaceutical tracers for cardiac imaging, Journal of Nuclear Cardiology 25, 1204 (2018).

[2] R. A. Werner, J. T. Thackeray, J. Diekmann, D. Weiberg, J. Bauersachs, and F. M. Bengel, The Changing Face of Nuclear Cardiology: Guiding Cardiovascular Care Toward Molecular Medicine, J Nucl Med 61, 951 (2020).

[3] M. A. McAteer et al., Translation of PET radiotracers for cancer imaging: recommendations from the National Cancer Imaging Translational Accelerator (NCITA) consensus meeting, BMC Med 23, (2025).

[4] T. Watabe et al., Recent advances in theranostics and oncology PET: emerging radionuclides and targets, Ann Nucl Med 39, 909 (2025).

[5] J. D. Oldan, M. G. Pomper, R. A. Werner, T. Higuchi, and S. P. Rowe, The cutting edge: Promising oncology radiotracers in clinical development, Diagnostic and Interventional Imaging 105, 400 (2024).

[6] D. P. Frush et al., Recurrent medical imaging exposures for the care of patients: one way forward, Eur Radiol 34, 6475 (2024).

[7] M. Hosono, M. Takenaka, H. Monzen, M. Tamura, M. Kudo, and Y. Nishimura, Cumulative radiation doses from recurrent PET–CT examinations, The British Journal of Radiology 94, (2021).

[8] A. Al-Ibraheem et al., Implementation of Radiotheranostics: Challenges, Barriers, and IAEA-Driven Strategies for Sustainable Access, Seminars in Nuclear Medicine 55, 1032 (2025).

[9] S. B. Hansen and D. Bender, Advancement in Production of Radiotracers, Seminars in Nuclear Medicine 52, 266 (2022).

[10] S. D. Voss, SPECT/CT, PET/CT and PET/MRI: oncologic and infectious applications and protocol considerations, Pediatr Radiol 53, 1443 (2023).

[11] M. K. Singh, A review of digital PET-CT technology: Comparing performance parameters in SiPM integrated digital PET-CT systems, Radiography 30, 13 (2024).

[12] S. Surti and J. S. Karp, Update on latest advances in time-of-flight PET, Physica Medica 80, 251 (2020).

[13] Z. Cheng, P. Chen, and J. Yan, A review of state-of-the-art resolution improvement techniques in SPECT imaging, EJNMMI Phys 12, (2025).

[14] K. P. Willowson and D. L. Bailey, Evolving SPECT-CT technology, British Journal of Radiology (2024).

[15] Shapiro, J. H. (2008). Computational ghost imaging. In Physical Review A (Vol. 78, Issue 6). American Physical Society (APS).

[16] Y. Klein, O. Sefi, H. Schwartz, and S. Shwartz, Chemical element mapping by x-ray computational ghost fluorescence, Optica 9, 63 (2022).

[17] https://www.mankatoclinic.com/pet-ct/

[18] E. Cole, M. Stewart, R. Littich, R. Hoareau, and P. Scott, Radiosyntheses using Fluorine-18: The Art and Science of Late Stage Fluorination, CTMC 14, 875 (2014).

[19] P. B. Hoffer, J. Bernstein, and A. Gottschalk, Fluorescent techniques in thyroid imaging, Seminars in Nuclear Medicine 1, 379 (1971).

[20] I. O. Romero, Y. Fang, M. Lun, and C. Li, x-ray Fluorescence Computed Tomography (XFCT) Imaging with a Superfine Pencil Beam x-ray Source, Photonics 8, 236 (2021).

[21] T. Staufer and F. Grüner, Review of Development and Recent Advances in Biomedical x-ray Fluorescence Imaging, IJMS 24, 10990 (2023).

[22] Pittman, T. B., Shih, Y. H., Strekalov, D. V., & Sergienko, A. V. (1995). Optical imaging by means of two-photon quantum entanglement. In Physical Review A (Vol. 52, Issue 5, pp. R3429–R3432). American Physical Society (APS).

[23] Bromberg, Y., Katz, O., & Silberberg, Y. (2009). Ghost imaging with a single detector. In Physical Review A (Vol. 79, Issue 5). American Physical Society (APS).

[24] L. I. Rudin, S. Osher, and E. Fatemi, Nonlinear total variation based noise removal algorithms, Physica D 60, 259 (1992).

[25] H. G. J. Moseley, The high-frequency spectra of the elements, The London, Edinburgh, and Dublin Philosophical Magazine and Journal of Science 26, 1024–1034 (1913).

[26] Oyedotun, T. D. T. (2018). X-ray fluorescence (XRF) in the investigation of the composition of earth materials: a review and an overview. In Geology, Ecology, and Landscapes (Vol. 2, Issue 2, pp. 148–154). Informa UK Limited.

[27] Yatsuk, O., Ferretti, M., Gorghinian, A., Fiocco, G., Malagodi, M., Agostino, A., & Gulmini, M. (2022). Data from Multiple Portable XRF Units and Their Significance for Ancient Glass Studies. In Molecules (Vol. 27, Issue 18, p. 6068). MDPI AG.

[28] Bilo, F., Cirelli, P., & Borgese, L. (2024). Elemental analysis of particulate matter by x-ray fluorescence methods: A green approach to air quality monitoring. In TrAC Trends in Analytical Chemistry (Vol. 170, p. 117427). Elsevier BV.

[29] de Viguerie, L., Sole, V. A., & Walter, P. (2009). Multilayers quantitative X-ray fluorescence analysis applied to easel paintings. In Analytical and Bioanalytical Chemistry (Vol. 395, Issue 7, pp. 2015–2020). Springer Science and Business Media LLC.

[30] Pereira, M. O., Felix, V. S., Oliveira, A. L., Ferreira, D. S., Pimenta, A. R., Carvalho, C. S., Silva, F. L., Perez, C. A., Galante, D., & Freitas, R. P. (2021). Investigating counterfeiting of an artwork by XRF, SEM-EDS, FTIR and synchrotron radiation induced MA-XRF at LNLS-BRAZIL. In Spectrochimica Acta Part A: Molecular and Biomolecular Spectroscopy (Vol. 246, p. 118925). Elsevier BV.

[31] Orsilli, J., Galli, A., Bonizzoni, L., & Caccia, M. (2021). More than XRF Mapping: STEAM (Statistically Tailored Elemental Angle Mapper) a Pioneering Analysis Protocol for Pigment Studies. Applied Sciences, 11(4), 1446.

[32] A. N. Shugar and J. L. Mass, Handheld x-ray Fluorescence Spectrometry for Art and Archaeology (Leuven University Press, Leuven, 2012).

[33] K. Shaker et al., "Longitudinal In-Vivo X-Ray Fluorescence Computed Tomography With Molybdenum Nanoparticles," in IEEE Transactions on Medical Imaging, vol. 39, no. 12, pp. 3910-3919, Dec. 2020.

[34] Dominique Bazin; Eddy Foy; Solenn Reguer; Stéphan Rouzière; Barbara Fayard; Hester Colboc; Jean-Philippe Haymann; Michel Daudon; Cristian Mocuta. The crucial contribution of X-ray fluorescence spectroscopy in medicine. Comptes Rendus. Chimie, Microcrystalline pathologies: Clinical issues and nanochemistry, Volume 25 (2022)

[35] M. van Heel and M. Schatz, Fourier shell correlation threshold criteria, Journal of Structural Biology 151, 250 (2005).

[36] A. Ben-Yehuda, O. Sefi, Y. Klein, H. Schwartz, E. Cohen, R. H. Shukrun, and S. Shwartz, High-resolution computed tomography with scattered x-ray radiation and a single pixel detector, Commun Eng 3, (2024).

[37] Industrial 3D printing of electronics for manufacturing and AME. https://www.nano-di.com.

[38] M. Manni, D. Karpov, K. J. Batenburg, S. Shwartz, and N. Viganò, Noise2Ghost: Self-Supervised Deep Convolutional Reconstruction for Ghost Imaging. https://doi.org/10.48550/arXiv.2504.10288

[39] J. C. Larsson, C. Vogt, W. Vågberg, M. S. Toprak, J. Dzieran, M. Arsenian-Henriksson, and H. M. Hertz, High-spatial-resolution x-ray fluorescence tomography with spectrally matched nanoparticles, Phys. Med. Biol. 63, 164001 (2018).

[40] S. Kulpe, M. Dierolf, B. Günther, J. Brantl, M. Busse, K. Achterhold, F. Pfeiffer, and D. Pfeiffer, Spectroscopic imaging at compact inverse Compton x-ray sources, Physica Medica 79, 137 (2020).

# תקציר


מגוון רחב של מידע אבחוני ברפואה מתקבל כיום באמצעות רדיונוקלידים. למרות היותם מרכזיים ברפואה גרעינית בשיטות הדמיה כמו SPECT, PET וסינטיגרפיה, השיטות כרוכות במגבלות מובנות: מינון הקרינה מגביל בדיקות חוזרות, זמן מחצית חיים קצר של רדיונוקלידים ולוגיסטיקה מורכבת מגבילות את הגישה ומגדילות עלויות, והרזולוציה המרחבית היחסית נמוכה שלהן מחייבת לעתים קרובות שימוש משלים של CT או MRI. למרות שפלואורסצנציה של קרני רנטגן (XRF) הוכרה כחלופה לא רדיואקטיבית עוד בשנות ה-70, יישומה מסתמך על סריקות נקודתיות, מה שמוביל לזמני מדידה ארוכים שאינם פרקטיים בקנה מידה של איברים אנושיים. כתוצאה מכך, השיטה טם נוצלה להדמיה קלינית ישימה בקנה מידה זה.

בעבודה זו אני מציג הדגמת היתכנות ראשונה לחלופה לא-רדיואקטיבית המבוססת על פלואורסצנציה מקרני רנטגן בשילוב הדמיית רפאים חישובית (Computational Ghost Imaging), שיטת הדמיה הנשענת על תבניות הארה מרחביות במקום גילוי מרחבי ישיר. המידע המרחבי מקודד בתבניות הידועות ומשוחזר באופן חישובי מתוך הקורלציות בינן לבין אותות הפלואורסצנציה הנמדדים. אובייקט המטרה שעליו התבצעה ההדמיה הוא פנטום אנתרופומורפי המכיל דמה של בלוטת תריס המלאה בתמיסת יוד, המשמש כמודל להדמיית סמן לא-רדיואקטיבי בממדים רלוונטיים קלינית.

המערכת הניסויית מורכבת ממקור רנטגן, מסכת כסף שמכילה את תבניות ההארה, וגלאי SDD לאיסוף פלואורסצנציה של יוד בחלון האנרגיות של Kα (כ-28 keV). סדרה של תבניות מאירה את הפנטום, ועבור כל תבנית נמדדת כמות הפלואורסצנציה של יוד. השחזור מתבצע באמצעות Noise2Ghost, אלגוריתם הבנוי מרשת נוירונים קונבולוציונית בפיקוח עצמי שאינה דורשת תמונת אמת חיצונית. השתמשתי במדדי איכות כמותיים כמו CNR, MSE ו- FRC, להערכת נאמנות השחזור.

מעבר לתוצאות המוצגות כאן, אני מסביר כיצד ניתן ליישם את שיטת XRF-CGI באופן קליני. שיפורים ביעילות איסוף הפלואורסצנציה, התאמה ספקטרלית לקצה ספיגת היוד, והתקדמות בפיתוח אלגוריתמי שחזור תמונה המבוססים על למידת מכונה יכולים להפחית את זמני המדידה במספר סדרי גודל. שיפורים אלו מכוונים לעבר מסלול שהינו אפשרי עבור הדמיה לא רדיואקטיבית בקנה מידה של איברים אנושיים, עם זמני מדידה המתקבלים על הדעת מבחינה קלינית.

עבודה זו נעשתה בהדרכתו של

פרופ׳ שרון שוורץ

מהמחלקה לפיזיקה של אוניברסיטת בר-אילן

# אוניברסיטת בר-אילן

## דימות רפאים באמצעות פלואורסצנצית קרני רנטגן בקנה מידה של איברים אנושיים לצורכי אבחון נטול רדיואיזוטופים

אליהו לוינסון

עבודה זו מוגשת כחלק מהדרישות לשם קבלת תואר מוסמך
במחלקה לפיזיקה של אוניברסיטת בר-אילן

רמת גן תשפ״ו